Distinct low-frequency noise fingerprints of filamentary and interfacial switching in $La_2NiO_{4+\delta}$-based RRAM

Yingxin Li,[1,*,†] Demian Ranftl,[2,†] Aleksandra Koroleva,[3] Tristan Stadler,[2] Philipp Schreyer,[1] Taewook Kim,[1] Yu Duan,[1] Alexey Arzumanov,[1] Mónica Burriel,[3] Jens Müller,[2] Lambert Alff,[1] and Eszter Piros[1]

[1]*Advanced Thin Film Technology, Institute of Materials Science, Technische Universität Darmstadt, Alarich-Weiss-Straße 2, 64287 Darmstadt, Germany*

[2]*Institute of Physics, Goethe Universität, Max-von-Laue-Straße 1, 60438, Frankfurt am Main, Germany*

[3]*Université Grenoble Alpes, CNRS, Grenoble INP, LMGP, 38000 Grenoble, France*

(Received 24 March 2026; revised 10 June 2026; accepted 29 September 2026; published 29 October 2026)

This work investigates the noise characteristics of filamentary- and interfacial-type resistive random-access memory devices in a single material system based on $La_2NiO_{4+\delta}$, using low-frequency noise spectroscopy across different resistance states, read voltages, and device sizes. We observe a clear difference in the noise properties of the two device types: (i) filamentary devices exhibit overall elevated noise levels compared with the interfacial ones, (ii) the relative noise magnitude between high (HRS) and low resistance states (LRS) in the two device types is inverted: elevated noise is present in the HRS of filamentary devices and in the LRS of interfacial ones and vice versa, (iii) no area dependence of noise properties is observed for the filamentary devices, whereas interfacial devices show a size-dependent frequency exponent and noise magnitude scaling. For both switching mechanisms, a systematic two-stage noise suppression with increasing read voltages is observed, which is found to be correlated with the transition from ohmic to space-charge-limited conduction. Our study links noise characteristics to the underlying switching and conduction mechanisms of oxygen vacancy migration-based memories.

DOI: 10.1103/z81t-dr2y

I. INTRODUCTION

With the explosive growth of digital data and accelerated development of artificial intelligence, significant demands have been imposed on the capacity of data storage, computational speed, and energy efficiency [1]. However, the traditional *von Neumann* architecture is approaching its fundamental limitations. Therefore, memory technologies capable of supporting in-memory computing [2] and neuromorphic computing [3–5] are highly sought after to overcome this bottleneck. Among emerging memory technologies, resistive random-access memory (RRAM) is considered a promising candidate for nonvolatile memory, taking advantage of its superior scalability, low power consumption, fast switching, and complementary metal-oxide-semiconductor (CMOS) compatibility [6]. The functional oxide layer can be selected from binary oxides such as HfO_2, TiO_2, Ta_2O_3, and Y_2O_3 [7–10]. In addition, ternary perovskite oxide materials such as $SrTiO_3$, $LaMnO_3$, $Pr_{0.7}Ca_{0.3}MnO_3$, or $La_2NiO_{4+\delta}$ [11–14] have demonstrated promising stable resistive switching behavior.

As a mixed ionic electronic conducting oxide, $La_2NiO_{4+\delta}$ exhibits excess oxygen and can accommodate a wide range of oxygen stoichiometries. Additionally, long-term potentiation/depression (LTP/LTD) and spike-timing-dependent plasticity behaviors have been demonstrated in $La_2NiO_{4+\delta}$-based RRAM devices, making them a promising candidate for artificial synapses in neuromorphic architectures [15]. Previously, a postannealing process has been shown to effectively tune the resistivity of the $La_2NiO_{4+\delta}$ film and modify the switching mode of $La_2NiO_{4+\delta}$-based RRAM devices [16]. Annealing in an inert (Ar) atmosphere increases the initial resistance of the device, resulting in filamentary switching behavior with a soft forming. In contrast, annealing in an oxidizing (O_2) atmosphere enhances the film's conductivity and leads to forming-free switching with the LRS and HRS resistances showing a device area dependence, indicating interfacial-type switching. Although both switching modes exhibit resistive switching behavior, their underlying mechanisms are fundamentally different.

In filamentary-type RRAM, a conductive filament forms within the oxide layer, where resistive switching

*Contact author: yingxin.li@tu-darmstadt.de
†These authors contributed equally to this work.

Published by the American Physical Society under the terms of the Creative Commons Attribution 4.0 International license. Further distribution of this work must maintain attribution to the author(s) and the published article's title, journal citation, and DOI.

is achieved through the filaments' growth and rupture [17]. Because of the filamentary nature of this switching mechanism, no significant variance in resistance is expected for differing electrode areas [18]. In contrast, interfacial-type RRAM operates without the formation of localized conductive paths. Instead, resistive switching is predominantly governed by the migration of oxygen ions, which modulate the potential barrier at the metal-oxide interface [3]. Typically, a gradual switching is observed in interfacial-type switching, making them suitable for analog applications [19,20]. In both switching modes, oxygen vacancies and oxygen interstitials play a critical role in device operation. However, these oxygen species also act as trap sites within the device [21,22]. Electron capture and emission at these traps induce two-level current fluctuations, so-called random telegraph noise (RTN), where the superposition of many such fluctuators results in $1/f$-type noise, ultimately degrading signal stability. Additionally, trap redistribution driven by thermal effects or electric stress during readout causes current variations, further increasing the overall noise level. Both processes contribute to reliability and variability issues of RRAM, posing significant challenges for its practical application [23].

Fluctuation (noise) spectroscopy [24] is an essential nondestructive tool for recording noise characteristics of a signal, probing conduction dynamics and trap states and providing valuable insight into trap-mediated fluctuations during device operation. This in turn helps to a deeper understanding of conduction mechanisms, switching dynamics, and trap-related activities in RRAM devices [25–28]. In this study, low-frequency noise (LFN) measurements are employed on devices presenting two different switching modes, aiming to systematically compare noise characteristics of filamentary- and interfacial-type RRAM across various parameters.

II. EXPERIMENTAL

The memristive devices investigated in this study adopt a typical metal-insulator-metal architecture consisting of $\mathrm{TiN}(100\,\mathrm{nm})/\mathrm{TiN}_x\mathrm{O}_{1-x}(2\text{–}3\,\mathrm{nm})/\mathrm{La_2NiO}_{4+\delta}(30\,\mathrm{nm})/\mathrm{Pt}(100\,\mathrm{nm})$ layers, as illustrated in Fig. 1. Following the sputtering of the Pt bottom electrode, a 30-nm-thick $\mathrm{La_2NiO}_{4+\delta}$ was grown by pulsed-injection metal-organic chemical vapor deposition. Both samples studied in this work were fabricated from the same deposition batch under identical deposition conditions, thereby minimizing sample-to-sample variations arising from the deposition process. The detailed deposition parameters can be found in the previous work [15]. After deposition, both samples are postannealed under different atmospheres, resulting in either filamentary-type (in Ar) or interfacial-type (in $\mathrm{O_2}$) switching devices [16]. Device patterning was performed using laser lithography (Heidelberg Instruments μPG 101), followed by the deposition of a 100-nm-thick TiN layer by reactive sputtering. The subsequent lift-off process

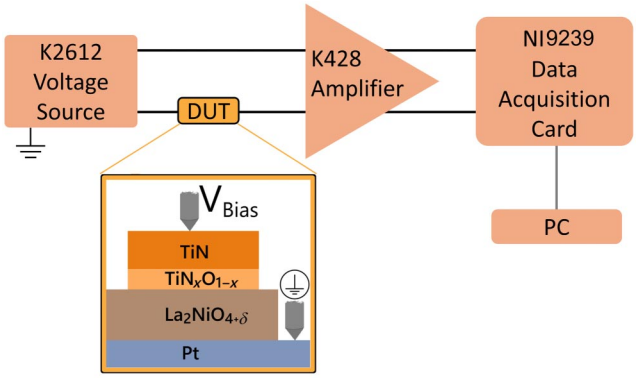

FIG. 1. Schematic representation of the two-terminal dc current noise measurement setup. A Keithley 2612 is used to apply a bias voltage to the device under test (DUT). The current signal is then amplified by a Keithley 428 current amplifier and transformed into a voltage signal. A National Instruments data acquisition card is used to record the signal before being transferred to a PC, where it can be further processed to obtain the noise spectra. A schematic representation of the DUT stack is displayed below the block diagram.

enabled the fabrication of devices with well-defined lateral dimensions ranging from 50×50 to $100 \times 100\ \mu\mathrm{m}^2$. A thin $\mathrm{TiN}_x\mathrm{O}_{1-x}$ interlayer spontaneously forms at the interface between the $\mathrm{La_2NiO}_{4+\delta}$ and TiN layers after the sputtering of the TiN top electrode [15].

Before LFN investigation, DUT is precharacterized and prepared with a Keithley 4200 semiconductor characterization system. For devices with a lateral dimension of $50 \times 50\ \mu\mathrm{m}^2$, the filamentary-type devices exhibit an initial resistance of approximately 155 kΩ, whereas the interfacial-type devices show an initial resistance of approximately 5 kΩ ($V_{\mathrm{read}} = 0.1$ V). The higher initial resistance of the filamentary-type devices is attributed to the lower hole carrier concentration and the expected higher work function of the $\mathrm{La_2NiO}_{4+\delta}$ film with lower oxygen content [16]. Resistive switching was subsequently initiated by applying bipolar current-voltage ($I-V$) switching cycles, with the voltage swept according to the sequence 0, +V, 0, −V, 0. For the filamentary-type devices, a maximum voltage of ±2.7 V was applied, resulting in mean LRS and HRS resistance values of approximately 2 and 55 kΩ, respectively ($V_{\mathrm{read}} = 0.1$ V). For the interfacial-type devices, a slightly higher maximum voltage of ±3.3 V was used to achieve reliable switching, resulting in mean LRS and HRS resistance values of approximately 2.5 and 30 kΩ, respectively. The compliance current for both samples was limited to 0.1 A. The detailed electrical characteristics of the two switching types have been systematically compared and discussed in our previous work [16]. Then, by utilizing a two-terminal LFN measurement setup, fluctuating current signals are recorded for noise investigation. Before each noise measurement, 3–5 switching cycles were performed for proper

device initialization. The DUT was subsequently programmed into the LRS or HRS by applying the corresponding set (negative) or reset (positive) voltage sweep. The use of an identical layer stack for both switching modes thereby allows for a direct comparison of their noise behavior. As shown in Fig. 1, during LFN measurement, bias voltages are applied using a Keithley 2612 source meter connected to the DUT. Current signals from the DUT are then amplified through a Keithley 428 current amplifier and converted into voltage signals. These voltage signals undergo digitization via an NI data acquisition card before being transferred to a PC for computational analysis, allowing extraction of noise spectra and amplitude characteristics [29]. Readout voltages ranging from 50 to 1000 mV are applied to study the bias dependence of the noise behavior. Additionally, devices of multiple lateral dimensions, spanning 50×50, 70×70, 85×85, and 100×100 μm^2, are analyzed.

A. Noise spectroscopy

Noise spectroscopy is a sensitive technique to study low-frequency dynamics of charge carriers in condensed matter systems. Usually, for a noisy voltage or current signal in the time domain, $\delta V(t)$ or $\delta I(t)$, the noise power spectral density (PSD) $S_{V,I}(f)$, is calculated. It quantifies how much power is associated with different parts of the frequency spectrum and is the Fourier transform of the system's autocorrelation function which describes the microscopic kinetics of the charge carriers coupled to equilibrium and nonequilibrium thermodynamic fluctuations [24]. Considering current fluctuations, $S_I(f)$ is defined as

$$S_I(f) = 2 \lim_{T\to\infty} \frac{1}{T} \left| \int_{-T/2}^{T/2} \delta I(t) e^{-i2\pi f t} dt \right|^2, \tag{1}$$

where $\delta I(t) \equiv I(t) - \langle I \rangle$ represents the fluctuation part of the current signal.

In many materials, the observed noise follows a $1/f^\alpha$ dependence (so-called $1/f$-type noise), often modeled as a superposition of independent two-level fluctuators (RTN). Each individual fluctuator contributes a Lorentzian-shaped spectrum:

$$S_I(f) = \langle (\delta I)^2 \rangle \frac{4\tau}{1 + (2\pi f \tau)^2}, \tag{2}$$

where τ is the characteristic (effective) time constant of the process related to the so-called corner frequency by $2\pi f_c = 1/\tau$. A superposition of Lorentzian spectra, Eq. (2), with a distribution of time constants $D(\tau) = D_0/\tau$ (corresponding to a uniform distribution of energies in thermally activated switching processes) would result in a pure $1/f$ spectrum:

$$S_I(f) = 4\langle (\delta I)^2 \rangle D_0 \int_{\tau_{\min}}^{\tau_{\max}} \frac{1}{1 + (2\pi f \tau)^2} d\tau \approx \frac{\langle (\delta I)^2 \rangle D_0}{f}, \tag{3}$$

for $2\pi f \tau_{\min} \ll 1 \ll 2\pi f \tau_{\max}$. Shifts of spectral weight of $S(f) \propto 1/f^\alpha$ to higher and lower frequencies with $\alpha < 1$ and $\alpha > 1$, respectively, often result from a nonuniform distribution of activation energies.

B. Fitting noise spectra

For practical analysis, see [29], measured time signals are converted into spectral data following the definition of the PSD, Eq. (1). For this process, time data are binned into multiple sections before being transformed to get an average PSD for each frequency window, with an upper limit of 250 Hz and a lower limit defined by the measurement time divided by the number of bins. The resulting $S(f)$ is typically plotted in a double-logarithmic representation.

If the spectrum is of $1/f$-type without a dominant Lorentzian contribution, it is fitted with a linear function in logarithmic space, assuming $S(f) \propto 1/f^\alpha$ dependence:

$$\log S(f) = -\alpha \log f + A, \tag{4}$$

where A is a constant representing the noise magnitude at 1 Hz.

If a single two-level fluctuator dominates the noise PSD, a Lorentzian spectrum becomes superimposed on the underlying $1/f$-type behavior, which requires two more fitting parameters, namely the noise magnitude and effective frequency (corner frequency f_c) of the two-level process.

III. RESULTS AND DISCUSSION

A. LFN read voltage scaling

Aiming at a systematic investigation of the voltage-dependent noise behavior, current signals are each recorded for 30 min at eight different readout voltages (V_{read}), ranging from 50 to 1000 mV, for both HRS and LRS. For both types of samples, the normalized noise level, here expressed as S_I/I^2, exhibits a similar downscaling trend with voltage. The noise spectra of a filamentary-type device in the HRS are shown as a representative example in Fig. 2(a). Since most devices exhibit $1/f^\alpha$-type low-frequency noise spectra, PSD at 1 Hz is extracted to quantify the noise magnitude at a given operating state. By plotting $S_I/I^2(f = 1\text{ Hz})$ as a function of voltage on a double-logarithmic scale, a general two-stage voltage dependence can be observed for both HRS and LRS for both switching mechanisms [Figs. 2(b) and 2(c)]. The noise amplitude initially decreases moderately at lower voltages. After a characteristic kink point at around 200 mV, the noise level decreases more strongly.

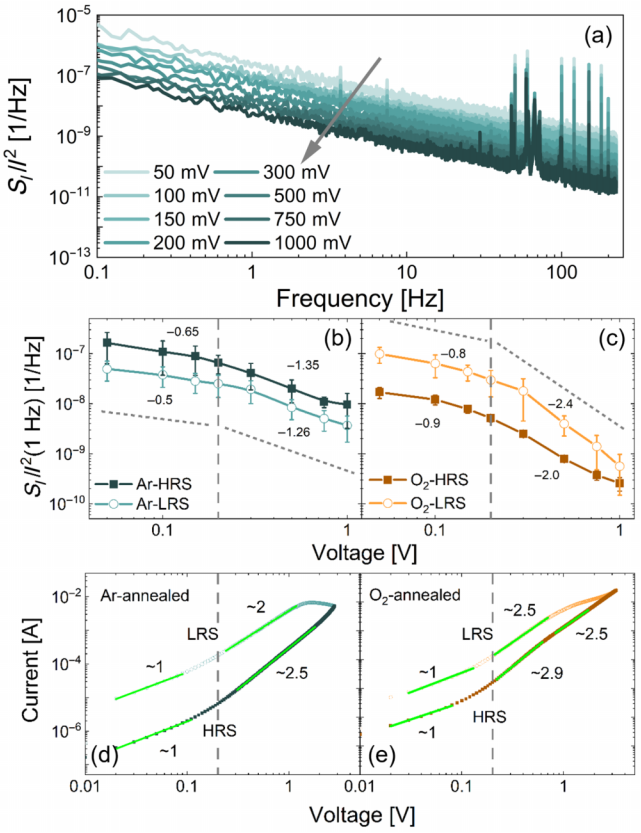

FIG. 2. (a) Representative noise spectra at eight readout voltages in HRS of a filamentary-type sample with a size of 50×50 μm^2. Voltage dependence of S_I/I^2 (1 Hz) for (b) filamentary-type switching and (c) interfacial-type switching in both states. Double-logarithmic plots of $I-V$ characteristics in positive polarity within the noise measurement window for (d) filamentary-type switching and (e) interfacial-type switching. The values near the curves denote the slope of the line fitted to the curve for each section. The dashed line marks the characteristic transition point at 200 mV, highlighting the clear correlation between the noise magnitude and conduction mechanism.

Remarkably, the scaling tendency of noise exhibits a clear correlation with the conduction mechanism of both samples. As shown in Figs. 2(d) and 2(e), the current-voltage ($I-V$) characteristics in the positive polarity plotted on a double-logarithmic scale show good agreement with the space-charge-limited-conduction (SCLC) model for both samples [30]. The full range $I-V$ curves of the two samples are displayed in Supplemental Material [31]. For both samples, a gradual transition from ohmic conduction ($I \propto V$) to trap-controlled SCLC conduction ($I \propto V^m$ with $m \geq 2$) appears at around 200 mV, suggesting a gradual filling of the exponentially distributed trap states in the bandgap with increased bias [32–34]. The larger exponent (slope m) in the interfacial-type devices further suggests a more progressive trap filling with increased voltage. For the noise amplitude, the coincidence of the transition from ohmic conduction to trap-controlled SCLC with the more strongly decreasing noise level indicates a trap-dominated behavior for both filamentary- and interfacial-type samples. Within the ohmic conduction region, the trap-filling effect is minimal, and consequently, no significant variation of the noise level can be detected. At higher voltages, however, continuous trap filling in the trap-controlled SCLC region reduces the density of active trap states, thereby lowering the probability of electron capture. As a result, the noise level decreases more strongly with increasing voltage. Evidently, the bias scaling of the noise magnitude is even more pronounced in the interfacial-type sample, consistent with the steeper slopes in the $I-V$ curves, indicating a more progressive reduction in the effective trap density in this sample. The observed correlation between the noise-scaling behavior and the conduction mechanism highlights LFN characterization as an effective tool for investigating the electronic conduction properties of RRAM devices.

B. Switching mechanisms and noise amplitude

In Figs. 3(a) and 3(b), the noise spectra of two switching modes are compared at three different voltages (150, 300, and 500 mV) in both HRS and LRS obtained in devices with an electrode area of 50×50 μm^2. In both states, the filamentary-type devices show an overall higher noise amplitude compared with interfacial-type devices.

As discussed in the previous section, the dominant noise in both samples is caused by trap-related phenomena. Electron capture and emission at trap sites lead to the formation and release of Coulomb blockade regions, which in turn lead to pronounced conductance fluctuations [35]. However, not all traps within the device contribute to the conductance fluctuation equally. The most significant fluctuations originate from traps in close proximity to the conduction pathway. In the case of filamentary-type switching, a localized narrow conductive filament forms within the oxide layer, which is more sensitive to local disturbances [36]. As illustrated in Fig. 3(e), once a trap is filled in the vicinity of the filament, the resulting Coulomb blockade effect can directly influence the overall conduction by partially or even completely obstructing the conduction path. Electron capture and emission in such traps result in substantial fluctuations of the total conductance. Contrary to filamentary-type devices, in interfacial-type switching, conduction takes place uniformly throughout the entire device [Fig. 3(f)]. Therefore, current disturbances caused by individual contributors are less pronounced, resulting in an overall lower S_I/I^2, since uncorrelated fluctuations in different paths with no common segment more likely cancel each other out on average [24].

Additionally, the values of $S_I/I^2(f = 1\ \text{Hz})$ in HRS and LRS are compared in Figs. 3(c) and 3(d), revealing different relationships for the two switching modes. In filamentary-type devices, a higher noise amplitude is

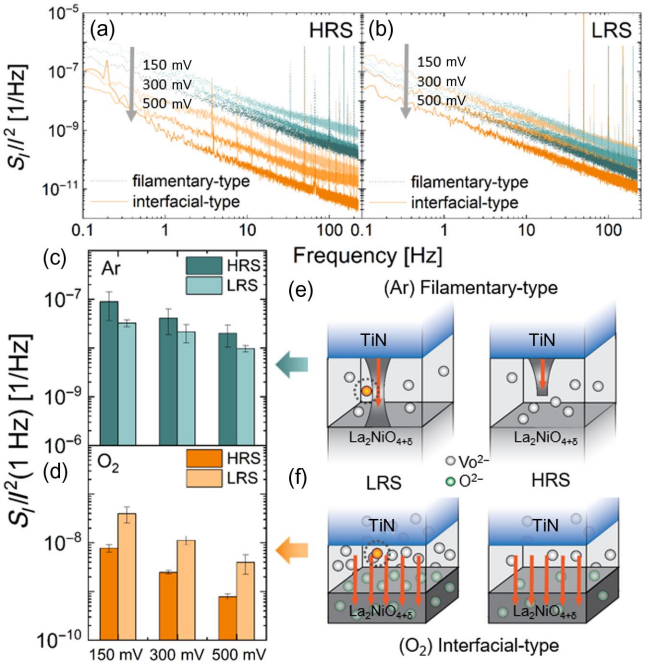

FIG. 3. Comparison of noise spectra for filamentary-type (Ar-annealed) and interfacial-type (O_2-annealed) switching at 150, 300, and 500 mV in (a) HRS and (b) LRS measured in 50×50 μm^2 devices. Comparison of $S_I/I^2(f = 1\ \text{Hz})$ between HRS and LRS for (c) filamentary-type and (d) interfacial-type switching. At each resistance state, at least four devices were measured for both samples, with the error bars indicating the device-to-device variations. Simplified schematic illustration of the (e) filamentary-type and (f) interfacial-type switching mechanism in $TiN/La_2NiO_{4+\delta}/Pt$ devices. The red arrows indicate the conduction pathways for each switching type. The white spheres represent the oxygen vacancies and green the oxygen interstitials. Active traps influencing conduction are depicted in orange, with dashed circles denoting the Coulomb blockade region they induce.

detected in the HRS compared with the LRS [Fig. 3(c)]. This observation has been consistently reported in filamentary-type RRAM devices in various material systems [26,37,38] and is commonly attributed to the formation of a gap between the filament and the electrode [Fig. 3(e)]. Different from LRS, the primary origin of noise in the HRS is believed to be the presence of random hopping pathways within the gap, significantly increasing the stochasticity of charge transport [39]. As a result, the current signal shows a higher instability compared with the LRS. In contrast, in interfacial-type devices, the redistribution of oxygen species during switching leads to variations in the probability of electron capture. As illustrated in Fig. 3(f), during the "set" process, oxygen ions migrate back into the $La_2NiO_{4+\delta}$ layer, increasing the density of oxygen vacancies within the TiN_xO_{1-x} layer. The accumulation of both, oxygen vacancies in TiN_xO_{1-x} and oxygen interstitials in $La_2NiO_{4+\delta}$, decreases the series resistance of the devices, which drives the device from the HRS into the LRS [33]. However, a substantial increase of trap density within the current path greatly increases the likelihood of charge capture. Therefore, the LRS exhibits significantly higher noise than the HRS in interfacial-type devices. The observed difference in noise amplitudes between resistance states of filamentary and interfacial RRAM devices is consistent with our understanding of the two distinct switching mechanisms and the major noise sources.

C. LFN area dependence

LFN is investigated for both switching modes in devices with various top electrode lateral dimensions, ranging from 50×50 to 100×100 μm^2. In Fig. 4, representative noise spectra of different device sizes in both HRS and LRS are shown for $V_{\text{read}} = 300$ mV. As for the area scaling, the noise amplitude of filamentary-type switching shows minimal to no dependence on device area [Figs. 4(a) and 4(b)], with an overall $1/f^{\alpha}$ noise with α close to 1 in both states. Such consistent noise characteristics, including noise amplitude and frequency scaling behavior, observed across various sizes of filamentary-type devices strongly support the localized nature of conduction. As the geometry of a localized filament is independent of the devices' lateral dimensions, electrode area scaling does not alter the amount or nature of traps affecting the conduction, thereby leaving the overall noise characteristics unaffected. In contrast, noise in interfacial-type devices exhibits a clear area dependence. As seen in Figs. 4(c) and 4(d), the normalized noise level $S_I/I^2(f)$ of the interfacial-type

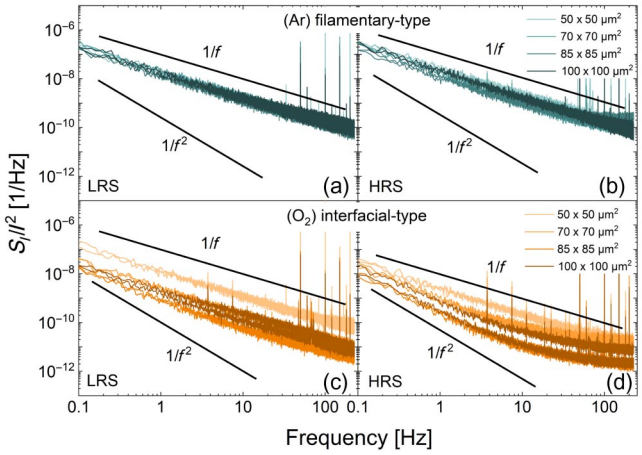

FIG. 4. Noise spectra for different device sizes for the (a) LRS and (b) HRS of the filamentary-type devices and for the (c) LRS and (d) HRS of the interfacial-type devices. In each panel, spectra from two separate devices are shown for each of the four device sizes (50×50, 70×70, 85×85, and 100×100 μm^2), demonstrating good measurement reproducibility. The reference lines of $1/f$ and $1/f^2$ serve as intuitive indicators of the frequency dependence $V_{\text{read}} = 300$ mV.

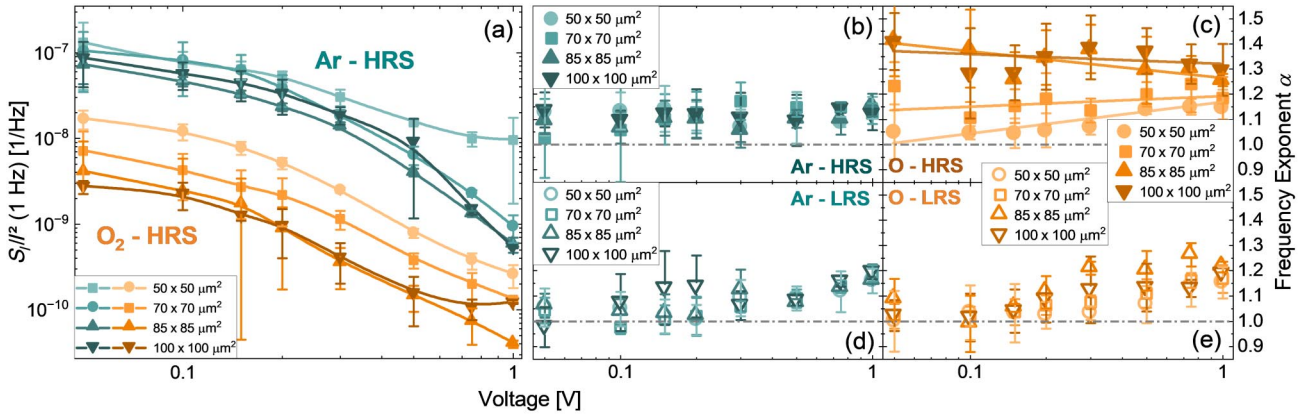

FIG. 5. Area dependent noise characteristics of filamentary-type (Ar-annealed) and interfacial-type (O_2-annealed) devices: (a) $S_I/I^2(1\ \mathrm{Hz})$ vs voltage in HRS of different device sizes. (b)–(e) Extracted frequency exponent α vs voltage for different device sizes of filamentary-type (Ar-annealed) and interfacial-type (O_2-annealed) devices in both HRS and LRS.

sample scales inversely with an increase in device size in both states. Notably, while the slope of the spectra remains similar in the LRS, a larger frequency exponent α, corresponding to a shift of spectral weight to lower frequencies, is observed in devices larger than $50 \times 50\ \mu m^2$ in the HRS. The area-dependent decrease of the noise amplitude is also found in other material systems such as TiO_2/HfO_2 bilayer RRAM [26] and can be explained by the bulk effect. The increased conductivity in larger devices dilutes the relative impact of individual fluctuators on the total conductance, which, in turn, reduces the overall noise amplitude. Simple statistical considerations predict an inverse scaling of the magnitude of the fluctuations with the size of the system [24]. However, this apparent noise suppression with increasing device sizes seems to become diminished as the device size approaches $100 \times 100\ \mu m^2$. This could be related to the similar resistances of devices of size 85×85 and $100 \times 100\ \mu m^2$ [16].

In Fig. 5, the statistical evaluation of the noise PSD and the frequency exponent α is presented, where both parameters of various device sizes are plotted as a function of V_{read}. Figure 5(a) shows the PSD comparison for both samples in the HRS; the corresponding results for devices in the LRS are provided in Supplemental Material [31]. Here, a systematic reduction of the normalized noise magnitude is observed with increasing bias for both device types. In combination with the conduction mechanism analysis presented in Sec. III A, an optimal read voltage window for maximum noise suppression and minimal power consumption can be determined, which is in this case in the range of approximately 200–500 mV. In addition, a roughly constant frequency exponent, for V_{read} between 50 and 1000 mV, is observed in the HRS of filamentary-type devices, as shown in Fig. 5(b). As the value of α is directly linked to the energy distribution of traps, the rather similar α values for different filamentary-type device sizes imply that neither V_{read} nor device size alters the energy distributions of traps in the HRS. In an ideal system with a broad and uniform distribution of time constants, noise magnitude scales linearly with inverse frequency, with α equal to 1. With slower (faster) fluctuation events becoming dominant in a system, an increase (decrease) of low-frequency components leads to a steepening (flattening) of the spectrum, where $\alpha > 1$ ($\alpha < 1$). The increase of α observed in the LRS at higher voltages, for both the filamentary- and interfacial-type devices [Figs. 5(d) and 5(e)] can therefore be attributed to a small but measurable shift in energy distribution $D(E)$ after progressive trap filling at elevated bias, as discussed in Sec. III A. Another possibility could be the promoted migration of oxygen species at higher voltages, which could affect $D(E)$. Furthermore, in the HRS of interfacial-type devices, α shows an additional overall increase with device size, approaching 1.4 for the largest device ($100 \times 100\ \mu m^2$). This increase reflects an enhanced spectral weight at low frequencies and a stronger contribution of low-frequency fluctuations in the larger interfacial-type devices. Moreover, these slower fluctuation events are playing a more dominant role in the HRS compared with the LRS. This observation may be associated with oxygen species diffusion and redistribution, which introduce longer characteristic time constants, resulting in enhanced low-frequency spectral weight in the HRS. In contrast, transport in the LRS may be dominated by more localized trapping and detrapping events with a homogeneous distribution of time constants, giving rise to a frequency dependence closer to conventional $1/f$ noise.

IV. CONCLUSION

In this study, we carried out a systematic comparison of the noise behavior in filamentary- and interfacial-type memristive devices in a single material system based on $La_2NiO_{4+\delta}$. By changing the annealing atmosphere, either filamentary-(Ar-annealing) or interfacial-type (O_2-annealing) switching is induced. Electronic fluctuations were investigated in both

device types as a function of lateral device sizes, readout voltages, and resistance states.

The two switching mechanisms display distinctly different noise characteristics. The narrow, localized conduction path in filamentary devices is more sensitive to local disturbances, thereby leading to an overall higher noise magnitude in both HRS and LRS as compared with interfacial devices. Also, due to the different distribution of traps with respect to the conduction path(s) in the two device types, we observe an opposite relation between the relative noise magnitude in the HRS and LRS. In filamentary-type switching, noise is enhanced in the HRS due to the formation of an insulating gap in the conduction path. In contrast, in interfacial-type devices the increased density of oxygen vacancies and oxygen interstitials within the layer stack enhances the probability of electron trapping and detrapping, resulting in a higher noise magnitude in the LRS. Moreover, the filamentary devices show no electrode area dependence in either the noise magnitude or the frequency exponent, while a clear inverse scaling of the normalized noise PSD with device size is observed in interfacial-type devices at all measured voltages. For both switching types, the LRS exhibits similar frequency exponents across various voltages, whereas in the HRS, slightly enhanced values of α in larger interfacial-type devices suggest a shift in the dominant noise source toward slower fluctuation events.

In addition, we show that the change in noise behavior of both device types, namely a two-stage scaling of the noise amplitude with the readout voltage, can be correlated with the transition from ohmic to SCLC conduction mechanism. A clear voltage scaling of noise amplitude highlights the connection between conduction mechanism and noise characteristics of RRAM devices. Furthermore, the systematic reduction of the noise levels in the HRS of both devices with increasing read voltages serves as a practical guide for determining the proper range of operating voltages for optimized noise behavior.

Overall, our results indicate that low-frequency noise characteristics serve as a quantifiable indicator for distinguishing filamentary switching from interfacial-type switching, providing a foundation for investigating trap-related effects and fluctuation phenomena across different switching mechanisms and facilitating future enhancements in the reliability and performance of memristive devices.

ACKNOWLEDGMENTS

Funding was received within the ECSEL Joint Undertaking projects WAKeMeUP and StorAIge in collaboration with the European Union's H2020 Framework Program (H2020/2014-2020) and National Authorities, under Grant No. 783176 and 101007321 respectively. Funding from the project NeAIxt is gratefully acknowledged. This project has received funding from the European Union's Horizon Europe research and innovation programme under the HORIZON-JU-Chips-2024-1-IA grant agreement No 101194172. The project is also supported by its members France, Italy, Czech Republic, Germany, Sweden, Danmark, Greece, Spain, Netherland, Portugal, Turkey, Switzerland. Views and opinions expressed are however those of the author(s) only and do not necessarily reflect those of the European Union or CHIPS JU. Neither the European Union nor the granting authority can be held responsible for them. Also, this project has received financial support from the CNRS through the MITI interdisciplinary programs (SynConnect project). Funding by the Federal Ministry for Research, Technology and Aeronautics (BMFTR) under Contracts No. 16ESE0298, No. 16MEE0154, No. 16ME0908K, No. 16MME0594 is gratefully acknowledged. Moreover, this work was supported by DFG Grants No. AL 560/21-1, No. AL 560/27-1, No. AL560/30-1, and No. MU 2733/7-1 (Project No. 517733815).

DATA AVAILABILITY

The data that support the findings of this article are not publicly available. The data are available from the authors upon reasonable request.

[1] D. Ielmini and G. Pedretti, Resistive switching random-access memory (RRAM): Applications and requirements for memory and computing, Chem. Rev. **125**, 5584 (2025).

[2] C. Wang, G. Shi, F. Qiao, R. Lin, S. Wu, and Z. Hu, Research progress in architecture and application of RRAM with computing-in-memory, Nanoscale Adv. **5**, 1559 (2023).

[3] Q. Wan, M. T. Sharbati, J. R. Erickson, Y. Du, and F. Xiong, Emerging artificial synaptic devices for neuromorphic computing, Adv. Mater. Technol. **4**, 1900037 (2019).

[4] J. H. Yoon, Y.-W. Song, W. Ham, J.-M. Park, and J.-Y. Kwon, A review on device requirements of resistive random access memory (RRAM)-based neuromorphic computing, APL Mater. **11**, 090701 (2023).

[5] S. Spiga, A. Sebastian, D. Querlioz, and B. Rajendran, *Memristive Devices for Brain-Inspired Computing: From Materials, Devices, and Circuits to Applications-Computational Memory, Deep Learning, and Spiking Neural Networks* (Woodhead Publishing, Sawston, Cambridge, 2020).

[6] Z. Shen, C. Zhao, Y. Qi, W. Xu, Y. Liu, I. Z. Mitrovic, L. Yang, and C. Zhao, Advances of RRAM devices: Resistive switching mechanisms, materials and bionic synaptic application, Nanomaterials **10**, 1437 (2020).

[7] S. Yu, H.-Y. Chen, B. Gao, J. Kang, and H.-S. P. Wong, HfO_x-based vertical resistive switching random access memory suitable for bit-cost-effective three-dimensional cross-point architecture, ACS Nano **7**, 2320 (2013).

[8] J. Park, M. Kwak, K. Moon, J. Woo, D. Lee, and H. Hwang, TiO_x-based RRAM synapse with 64-levels of conductance and symmetric conductance change by adopting a hybrid pulse scheme for neuromorphic computing, IEEE Electron Device Lett. **37**, 1559 (2016).

[9] M.-J. Lee, C. B. Lee, D. Lee, S. R. Lee, M. Chang, J. H. Hur, Y.-B. Kim, C.-J. Kim, D. H. Seo, S. Seo *et al.*, A fast, high-endurance and scalable non-volatile memory device made from asymmetric Ta_2O_{5-x}/TaO_{2-x} bilayer structures, Nat. Mater. **10**, 625 (2011).

[10] S. Petzold, E. Piros, R. Eilhardt, A. Zintler, T. Vogel, N. Kaiser, A. Radetinac, P. Komissinskiy, E. Jalaguier, E. Nolot *et al.*, Tailoring the switching dynamics in yttrium oxide-based RRAM devices by oxygen engineering: From digital to multi-level quantization toward analog switching, Adv. Electron. Mater. **6**, 2000439 (2020).

[11] X. T. Zhang, Q. X. Yu, Y. P. Yao, and X. G. Li, Ultrafast resistive switching in $SrTiO_3$: Nb single crystal, Appl. Phys. Lett. **97**, 222117 (2010).

[12] I. Maity, A. K. Mukherjee, and A. D. Thakur, Enhanced stability and low operational voltage of resistive switching behavior in defect engineered $LaMnO_3$ film, Appl. Phys. A **129**, 11 (2023).

[13] A. Sawa, T. Fujii, M. Kawasaki, and Y. Tokura, Hysteretic current–voltage characteristics and resistance switching at a rectifying $Ti/Pr_{0.7}Ca_{0.3}MnO_3$ interface, Appl. Phys. Lett. **85**, 4073 (2004).

[14] T.-K. Khuu, G. Lefèvre, C. Jiménez, H. Roussel, A. Riaz, S. Blonkowski, E. Jalaguier, A. Bsiesy, and M. Burriel, $La_2NiO_{4+\delta}$-based memristive devices integrated on Si-based substrates, Adv. Mater. Technol. **7**, 2200329 (2022).

[15] T.-K. Khuu, A. Koroleva, A. Degreze, E.-I. Vatajelu, G. Lefèvre, C. Jiménez, S. Blonkowski, E. Jalaguier, A. Bsiesy, and M. Burriel, Analog memristive devices based on $La_2NiO_{4+\delta}$ as synapses for spiking neural networks, J. Phys. D **57**, 10LT01 (2024).

[16] A. Koroleva, T.-K. Khuu, C. Magén, H. Roussel, C. Jiménez, C. Ternon, E.-I. Vatajelu, and M. Burriel, Impact of the $La_2NiO_{4+\delta}$ oxygen content on the synaptic properties of the $TiN/La_2NiO_{4+\delta}/Pt$ memristive devices, Adv. Electron. Mater. **10**, 2400096 (2024).

[17] T. Wei, Y. Lu, F. Zhang, J. Tang, B. Gao, P. Yu, H. Qian, and H. Wu, Three-dimensional reconstruction of conductive filaments in HfO_x -based memristor, Adv. Mater. **35**, 2209925 (2023).

[18] D. J. Wouters, R. Waser, and M. Wuttig, Phase-change and redox-based resistive switching memories, Proc. IEEE **103**, 1274 (2015).

[19] Q. Wang, G. Niu, S. Roy, Y. Wang, Y. Zhang, H. Wu, S. Zhai, W. Bai, P. Shi, S. Song, Z. Song, Y.-H. Xie, Z.-G. Ye, C. Wenger, X. Meng, and W. Ren, Interface-engineered reliable HfO_2-based RRAM for synaptic simulation, J. Mater. Chem. C **7**, 12682 (2019).

[20] R. Yang, H.-M. Huang, Q.-H. Hong, X.-B. Yin, Z.-H. Tan, T. Shi, Y.-X. Zhou, X.-S. Miao, X.-P. Wang, S.-B. Mi *et al.*, Synaptic suppression triplet-STDP learning rule realized in second-order memristors, Adv. Funct. Mater. **28**, 1704455 (2018).

[21] J.-K. Lee, J.-W. Lee, J. Park, S.-W. Chung, J. S. Roh, S.-J. Hong, I.-W. Cho, H.-I. Kwon, and J.-H. Lee, Extraction of trap location and energy from random telegraph noise in amorphous TiO_x resistance random access memories, Appl. Phys. Lett. **98**, 143502 (2011).

[22] F. M. Puglisi, A. Padovani, L. Larcher, and P. Pavan, Random telegraph noise: Measurement, data analysis, and interpretation, in *2017 IEEE 24th International Symposium on the Physical and Failure Analysis of Integrated Circuits (IPFA)* (IEEE, New York, 2017), pp. 1–9.

[23] F. Zahoor, T. Z. Azni Zulkifli, and F. A. Khanday, Resistive random access memory (RRAM): An overview of materials, switching mechanism, performance, multilevel cell (MLC) storage, modeling, and applications, Nanoscale Res. Lett. **15**, 90 (2020).

[24] J. Müller, Noise and fluctuations in condensed matter systems, Contemp. Phys. **66**, 62 (2025).

[25] E. Piros, M. Lonsky, S. Petzold, A. Zintler, S. Sharath, T. Vogel, N. Kaiser, R. Eilhardt, L. Molina-Luna, C. Wenger *et al.*, Role of oxygen defects in conductive-filament formation in Y_2O_3-based analog RRAM devices as revealed by fluctuation spectroscopy, Phys. Rev. Appl. **14**, 034029 (2020).

[26] J.-K. Lee and S. Kim, Comparative analysis of low-frequency noise based resistive switching phenomenon for filamentary and interfacial RRAM devices, Chaos Solit. Fractals **173**, 113633 (2023).

[27] B. Sánta, Z. Balogh, L. Pósa, D. Krisztián, T. N. Török, D. Molnár, C. Sinkó, R. Hauert, M. Csontos, and A. Halbritter, Noise tailoring in memristive filaments, ACS Appl. Mater. Interfaces **13**, 7453 (2021).

[28] N. Kumar, J. E. Han, K. Beckmann, N. Cady, and G. Sambandamurthy, Noise spectroscopy and electrical transport in NbO_2 Memristors with dual resistive switching, Adv. Electron. Mater. **11**, 2400877 (2025).

[29] T. Thyzel, M. Kopp, J. Pieper, T. Stadler, and J. Müller, Methods in fluctuation (noise) spectroscopy and continuous analysis for high-throughput measurements, Meas. Sci. Technol. **36**, 015501 (2025).

[30] F.-C. Chiu, A review on conduction mechanisms in dielectric films, Adv. Mater. Sci. Eng. **2014**, 578168 (2014).

[31] See Supplemental Material at http://link.aps.org/supplemental/10.1103/z81t-dr2y for additional details on $I-V$ characteristics of both samples and normalized PSD at 1 Hz for four different device sizes.

[32] P. Zhang, Y. S. Ang, A. L. Garner, Á. Valfells, J. Luginsland, and L. Ang, Space-charge limited current in nanodiodes: Ballistic, collisional, and dynamical effects, J. Appl. Phys. **129**, 100902 (2021).

[33] T.-K. Khuu, A. Koroleva, C. Moncasi, A. Stangl, D. Cooper, G. Lefèvre, F. Wilhelm, A. Rogalev, M. Weber, C. Jiménez *et al.*, Operando spectroscopic investigation of the valence change mechanism in $La_2NiO_{4+\delta}$-based memristive devices, Adv. Electron. Mater. **11**, 2400313 (2025).

[34] P. Mark and W. Helfrich, Space-charge-limited currents in organic crystals, J. Appl. Phys. **33**, 205 (1962).

[35] F. M. Puglisi, P. Pavan, L. Vandelli, A. Padovani, M. Bertocchi, and L. Larcher, A microscopic physical description of RTN current fluctuations in HfO_x RRAM, in *IEEE Int. Reliab. Phys. Symp. Proc.* (IEEE, New York, 2015), p. 5B–5.

[36] F. M. Puglisi, N. Zagni, L. Larcher, and P. Pavan, Random telegraph noise in resistive random access memories: Compact modeling and advanced circuit design, IEEE Trans. Electron Devices **65**, 2964 (2018).

[37] S. Yu, R. Jeyasingh, Y. Wu, and H.-S. P. Wong, Characterization of low-frequency noise in the resistive switching of transition metal oxide HfO_2, Phys. Rev. B **85**, 045324 (2012).

[38] J. Heo, Y. Cho, H. Ji, M.-H. Kim, J.-H. Lee, J.-K. Lee, and S. Kim, Noise-assisted transport mechanism analysis and synaptic characteristics in $ZrO_x/HfAlO_x$-based memristor for neuromorphic systems, APL Mater. **11**, 111103 (2023).

[39] F. M. Puglisi, L. Larcher, A. Padovani, and P. Pavan, A complete statistical investigation of RTN in HfO_2-based RRAM in high resistive state, IEEE Trans. Electron Devices **62**, 2606 (2015).